Journal of *Marine Science and Engineering*

MDPI

Article

Sliding Mode Control of a Nonlinear Wave Energy Converter Model

Tania Demonte Gonzalez [1,*], Gordon G. Parker [1], Enrico Anderlini [2] and Wayne W. Weaver [1]

[1] Department of Mechanical-Engineering-Engineering Mechanics, Michigan Technological University, Houghton, MI 49931, USA; ggparker@mtu.edu (G.G.P.); wwweaver@mtu.edu (W.W.W.)
[2] Department of Mechanical Engineering, University College London, London WC1E 6BT, UK; e.anderlini@ucl.ac.uk
* Correspondence: tsdemont@mtu.edu

Abstract: The most accurate wave energy converter models for heaving point absorbers include nonlinearities, which increase as resonance is achieved to maximize the energy capture. Over the power production spectrum and within the physical limits of the devices, the efficiency of wave energy converters can be enhanced by employing a control scheme that accounts for these nonlinearities. This paper proposes a sliding mode control for a heaving point absorber that includes the nonlinear effects of the dynamic and static Froude-Krylov forces. The sliding mode controller tracks a reference velocity that matches the phase of the excitation force to ensure higher energy absorption. This control algorithm is tested in regular linear waves and is compared to a complex-conjugate control and a nonlinear variation of the complex-conjugate control. The results show that the sliding mode control successfully tracks the reference and keeps the device displacement bounded while absorbing more energy than the other control strategies. Furthermore, due to the robustness of the control law, it can also accommodate disturbances and uncertainties in the dynamic model of the wave energy converter.

Keywords: wave energy; nonlinear model; Froude-Krylov force; sliding mode control

Citation: Demonte Gonzalez, T.; Parker, G.G.; Anderlini, E.; Weaver, W.W. Sliding Mode Control of a Nonlinear Wave Energy Converter Model. *J. Mar. Sci. Eng.* **2021**, *9*, 951. https://doi.org/10.3390/jmse9090951

Academic Editors: Giuseppe Giorgi and Sergej Antonello Sirigu

Received: 4 August 2021
Accepted: 26 August 2021
Published: 1 September 2021

1. Introduction

Recently, the generation of electricity from ocean waves has gained special attention. Studies of the potential global market for wave power showed that the world's wave power resource is estimated to be two TW [1]. Additionally, waves have a very high power density, requiring smaller devices to capture the energy carried by the incoming waves. Wave energy can also improve energy security by complementing the output of other renewable energy sources, thus reducing the storage needs. However, although phased development has helped reduce risks, the wave energy sector is still in its infancy, with recent prototype wave energy converters (WECs) having a Levelized Cost of Energy (LCoE) in the range of \$120–\$470/MWh [2]. Hence, technological advances are required to reduce the LCoE 50–75% to enable the industry to leap from government-funded research to sustainable industrial competition within the energy market. Optimizing the control of WECs has been identified as one of the critical areas with the highest potential to improve the viability of wave energy [3], as the latest control methods can enhance power absorption by up to 20% while reducing structural loads.

Researchers have used well-established control methods in WECs that include Complex-Conjugate Control (CCC), Latching, and Model Predictive Control (MPC) [4]. In complex-conjugate control, optimal energy absorption is sought by tuning the power take-off (PTO) resistance and reactance to cancel the system's inherent hydrodynamic resistance and reactance [5]. This control strategy is conceptually simple and presents a low computational cost; however, it leads to excessive motions and loads of the WEC. This can be avoided by implementing alternative suboptimal control schemes that include

physical constraints on the motions and power of the device. Latching control is based on locking the device through dedicated mechanisms during a certain period of time of the wave oscillation cycle to achieve resonance of the WEC [6,7]. Resonance is achieved when the system is being excited at its natural frequency. While latching control solves the PTO limitation problem of CCC, it is prone to failure of the mechanical clamping pieces generating extra costs and reducing its reliability. MPC strategies maximize the energy absorbed by applying the optimal control force to achieve resonance at each time step over a future time horizon [8]. However, a prediction of the wave motion is required, and its complexity of implementation in real-time demands high computational requirements.

Most of these control techniques use the linear model developed by Cummins [9] with hydrodynamic parameters obtained from boundary element methods (BEM) due to their simplicity and high computational efficiency. Although linear models are effective for most ocean engineering applications where the aim is typically to stabilize the structure, linear models are inadequate for WEC control, where the primary objective is to amplify the device's motions to maximize the power absorption [10]. As a result, control strategies based on linear models are often suboptimal and lead to higher LCoE.

Nonlinear models often include the quadratic term of the pressure from the incident flow, the integration of the pressure forces over the instantaneous wetted surface of the device called Froude-Krylov (FK) forces, and the nonlinear incident flow potential [11]. Each of these nonlinearities adds an extra level of complexity and computational load. However, it is understood that nonlinear models are more accurate than linear models, particularly for buoy geometries with varying cross-sectional areas. A previous study [12] that compared different modeling options showed that the dominant sources of nonlinearities are likely to be the nonlinear Froude-Krylov forces for devices with a varying cross-sectional area.

While, in linear modeling, the FK forces are calculated over a constant wetted area of the device, in nonlinear models, the pressure is integrated over the instantaneous wetted surface area. This is generally done by implementing a very fine mesh or a remeshing routine of the surface, which requires more computational effort. As a result, the nonlinear model is more accurate but is very computationally expensive. However, in Reference [13], Giorgi et al. developed a computationally efficient analytical method to compute the nonlinear dynamic and static Froude-Krylov forces based on the instantaneous wetted surface area of the buoy. This analytical method presents only a 2% error compared to the more computationally expensive methods. Therefore, in this study, the nonlinear FK forces are incorporated using a variation of the algebraic solution proposed by Giorgi et al.

This paper proposes a second-order Sliding Mode Control (SMC) strategy that incorporates the nonlinear Froude-Krylov forces to reduce the discrepancies between the mathematical model and the actual system. In addition, this SMC is designed to track the desired reference signals using low computational efforts and rejecting disturbances encountered by the WEC or parametric errors presented in the model. The controller will be investigated in a simulation environment using a standard spherical WEC and regular waves.

Many researchers have studied SMC in oscillating water columns (OWC). A popular SMC for a nonlinear OWC is the super-twisting algorithm presented in [14]. This control strategy has been used in different configurations of OWCs, where it noticeably improved the electric power conversion compared to other strategies [15]. Sliding mode control has also been used to track underwater vehicles' positions [16] due to its robustness characteristics that allow for model uncertainties or environmental disturbances. In this paper, SMC is applied to a heaving point absorber. An SMC strategy for heaving WECs was proposed in Reference [17], where it was shown to provide a viable solution to increase energy extraction. The SMC was designed to track a reference velocity without violating the physical constraints of the device. The results showed that the SMC successfully tracked the reference signal even when system perturbations were present. However, this work was done using a linear approximation of the WEC's dynamic model. This study aims to

improve the energy extraction performance of WECs where its SMC can exploit the WEC's nonlinear model terms.

The main contributions of this study consist of first, the derivation of algebraic nonlinear Froude-Krylov forces based on the work of Giorgi et al., second, the application of an SMC to the nonlinear WEC model; and third, the design of a nonlinear variant of complex-conjugate control.

This paper is organized into six sections. First, the following section describes the general dynamics of a heaving WEC and the derivation of the nonlinear algebraic Froude-Krylov forces showing the first contribution mentioned above. Then, the second and third contributions are in Section 3, where the SMC strategy is designed and compared to a complex-conjugate control and a nonlinear variant of complex-conjugate control. In Section 4, the simulation used to evaluate closed-loop performance is described. Section 5 shows the results, and Section 6 provides conclusions and area for further study.

2. Model Description

Mathematical models for WECs are essential for the design of model-based control. These models are typically linear because of their low computational requirements, in which they assume small motions. However, there are situations in which the movement is not small while still producing power, and the nonlinearities of the device become significant.

The incoming waves are classified as linear and nonlinear depending on the wave steepness S, which is the ratio between the wave height h and the wavelength λ [18]. Waves are also classified as regular and irregular, where regular waves are characterized by a specific amplitude A, frequency ω_0, and wavelength, whereas irregular waves are composed of multiple frequency waves. In this paper, linear and regular waves are used, representing the wave free surface elevation $\eta(t)$ as a function of time only:

$$\eta(t) = Acos(\omega_0 t) \tag{1}$$

A floating single degree of freedom (SDOF) buoy is shown in Figure 1, where the lower part of the sphere is attached to a linear generator for power take-off (PTO), which is fixed to the seabed. The PTO subsystem converts the wave energy into electrical energy and energizes the system to track the reference profile. The excitation force is shown as $F_{exc}\ (t)$, and is composed of the hydrodynamic Froude-Krylov force and the diffraction force, the buoy's displacement from its equilibrium position is denoted $z\ (t)$, and the control force implemented by the PTO system is $F_c\ (t)$.

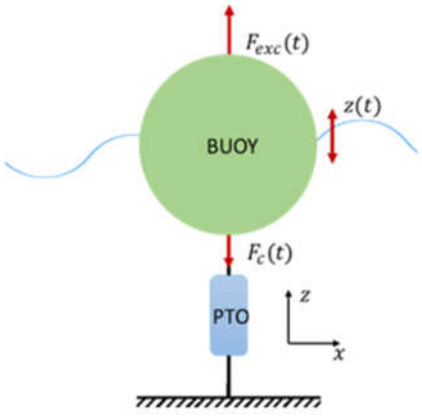

Figure 1. Heaving buoy with power take-off (PTO) fixed to the sea bed.

The general heaving WEC hydrodynamic model used in this paper is described as:

$$m\,\ddot{z}(t) = F_{FK} + F_d + F_R - F_c \tag{2}$$

where:

m: Mass of the buoy in the air
F_{FK}: Froude-Krylov Forces
F_d: Diffraction Force
F_R: Radiation Force
F_c: Control Force

2.1. Diffraction Force

The diffraction force is the force the incoming waves apply on the buoy as it is held fixed in the water [5]. It can be is represented as the convolution of the product of the wave free surface elevation and the diffraction impulse response function (*IRF*):

$$F_d = \int_{-\infty}^{+\infty} K_{d_{IRF}}(t-\tau)\,\eta(t)\,d\tau \tag{3}$$

where $K_{d_{IRF}}$ is the diffraction *IRF*.

When the buoy diameter is much smaller than the wavelength, the disturbance field generated by the body is small enough to be ignored [19]. Therefore, the diffraction force is neglected in the simulation of this paper. This force could also be accounted as a disturbance to the system.

2.2. Radiation Force

The radiation force can be interpreted as the force that the body experiences when it oscillates in calm water. It is common to divide this force into two parts: the added mass force, proportional to the body's acceleration $\ddot{z}(t)$, and the wave damping force, proportional to the body velocity $\dot{z}(t)$ [20]. Thus, the radiation force can be represented as:

$$F_R(t) = -\int_{-\infty}^{+\infty} K_{r_{IRF}}\,(t-\tau)\,\dot{z}(t)\,d\tau - m_a(\omega_\infty)\ddot{z}(t) \tag{4}$$

where:

$K_{r_{IRF}}$: Radiation *IRF*
$m_a(\omega_\infty)$: Added mass

Evaluating the convolution integral in the radiation force is very expensive to compute at every time step of the simulation, and it is not possible on a real-time application. However, when the buoy is exposed to only harmonic waves of frequency ω_0, the convolution in Equation (4) can be represented as:

$$F_R = c(\omega_0)\dot{z}(t) - m_a(\omega_\infty)\ddot{z}(t) \tag{5}$$

where $c(\omega_0)$ is the linear damping constant.

2.3. Froude-Krylov Forces

The Froude-Krylov forces F_{FK} are the hydrostatic force $F_{FK_{st}}$ and the hydrodynamic force $F_{FK_{dy}}$. The hydrostatic force is the difference between the gravity force F_g and the force caused by the hydrostatic pressure over the wetted surface of the buoy, and the hydrodynamic force is the integral of the unsteady pressure field over the wetted surface of the floating buoy caused by the incident waves.

$$F_{FK} = F_g - \iint P(t)\,\mathbf{n}dS \tag{6}$$

In linear models, the integration is done over the constant mean wetted surface, while in the nonlinear approach, the instantaneous wetted surface of the body is considered. This approach typically requires significant computational effort. However, Giorgi et al. proposed an algebraic solution that significantly reduces the computational effort for heaving axisymmetric geometries. The algebraic solution is found by defining the pressure

$P(t)$, the infinitesimal element of the surface $\mathbf{n}\, dS$, and the limits of integration. The total pressure for deep water waves can be found using Airy's wave theory.

$$P(t) = \rho g e^{\chi z} A cos(\omega t) - \rho g z(t) \tag{7}$$

where:

ρ: Density of water

g: Gravity acceleration constant

χ: Wavenumber

In Giorgi et al.'s work, the surface of the geometry of the buoy was defined in parametric cylindrical coordinates as:

$$\begin{cases} x(\sigma,\theta) = f(\sigma)\cos(\theta) \\ y(\sigma,\theta) = f(\sigma)\sin(\theta), \\ z(\sigma,\theta) = \sigma \end{cases} \qquad \theta \in [0, 2\pi) \wedge \sigma \in [\sigma_1, \sigma_2] \tag{8}$$

where $f(\sigma)$ is the profile of revolution of the point absorber. Using the radial e_σ and tangent e_θ vectors canonical basis, and only the vertical component for heave motion restriction, the infinitesimal surface element, and the pressure becomes:

$$e_\sigma \times e_\theta \, dS = \mathbf{n} \| e_\sigma \times e_\theta \| \, d\sigma d\theta = \mathbf{n}\, f(\sigma) \sqrt{f'(\sigma)^2 + 1}\, d\sigma d\theta$$

$$P_z(t) = P(t) \cdot \langle \mathbf{n}, \mathbf{k} \rangle = P(t) \cdot \frac{f\prime(\sigma)}{\sqrt{f'(\sigma)^2 + 1}} \tag{9}$$

Combining these equations, the Froude-Krylov forces are:

$$F_{FK} = F_g - \iint P(t) f'(\sigma) f(\sigma) d\sigma d\theta \tag{10}$$

The paper continues defining the limits of integration based on the free surface elevation and the draft of the buoy h_0 at equilibrium as:

$$\begin{cases} \sigma_1 = z_d(t) - h_0 \\ \sigma_2 = \eta(t) \end{cases} \tag{11}$$

where $z_d(t)$ is the vertical displacement of the buoy from equilibrium. For a spherical point absorber, the profile of revolution derived in Giorgi et al. paper is $f(\sigma) = \sqrt{R^2 - (\sigma - z_d)^2}$, where R is the radius of the buoy.

In this paper, the limits of integration and the profile of revolution have been redefined using calculus to derive the instantaneous wetted surface area of the sphere. Considering the bottom of the sphere as the lower limit of integration, the profile of revolution of the sphere at still water level (SWL) shown in Figure 2a is $f(\sigma) = \sqrt{R^2 - (-R + h_0 + \sigma)^2}$, where the SWL was used as a reference and the instantaneous wetted surface area is shaded in blue. In this case, the lower limit of integration is $-h_0$ and the upper limit is 0. When the buoy is displaced by $z_d(t)$, and the free surface elevation $\eta(t)$ is not zero as shown in Figure 2b the profile of revolution of the sphere becomes:

$$f(\sigma) = \sqrt{R^2 - (-R + h_0 - z_d(t) + \eta(t) + \sigma)^2} \tag{12}$$

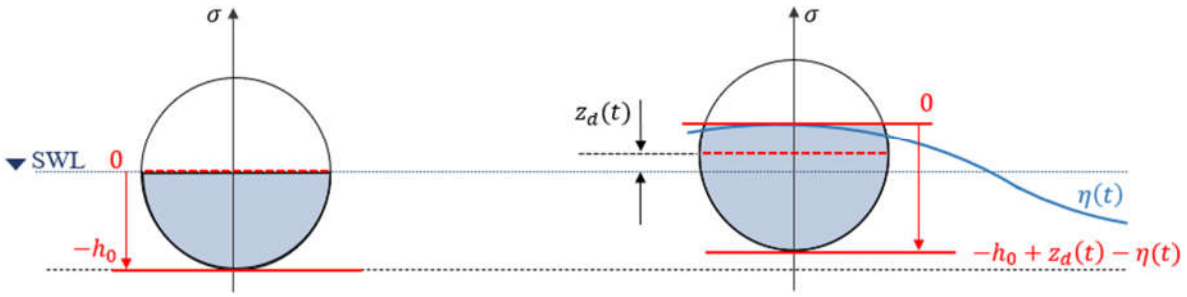

(**a**) (**b**)

Figure 2. Heaving spherical point absorber at the still water level (SWL) on the left (**a**); to the right (**b**) is shown the displacement from resting position $z_d(t)$ and the wave elevation $\eta(t)$.

The limits of integration are: 0 for the upper limit, and $l_b = -h_0 + z_d(t) - \eta(t)$ for the lower limit. Combining Equations (8)–(12), the integral of the Froude-Krylov forces of a heaving spherical buoy can be expressed as:

$$F_{FK_z} = F_g - 2\pi\rho g \int_{l_b}^{0} (e^{\chi z} A cos(\omega t) - \sigma)(-R + h_0 - z_d(t) + \eta(t) + \sigma)\, d\sigma \tag{13}$$

Solving the integral and separating the Froude-Krylov forces, the resulting nonlinear hydrostatic, and hydrodynamic forces of the system are:

$$F_{FK_{st}} = F_g + \frac{\pi\rho g}{3}(\eta(t) + h_0 - z_d(t))^2(3R - \eta(t) - h_0 + z_d(t)) \tag{14}$$

$$F_{FK_{dy}} = \frac{2\pi\rho g\eta(t)}{\chi^2}\left(e^{-\chi(\eta(t)+h_0-z_d(t))} + \chi\left(-R + \eta(t) + h_0 - z_d(t) + Re^{-\chi(\eta(t)+h_0-z_d(t))}\right) - 1\right) \tag{15}$$

The complete nonlinear model of a single degree of freedom WEC in heave mode can then be described as:

$$M\ddot{z}(t) = F_d + F_{FK_{st}} + F_{FK_{dy}} - c(\omega_0)\dot{z}(t) - F_c \tag{16}$$

where $M = (m + m_a(\omega_\infty))$.

For the subsequent control design, it will be convenient to write Equation (16) as:

$$\ddot{z}(t) = f_t(z(t), \dot{z}(t), \eta(t)) - \overline{F}_c \tag{17}$$

where f_t is the true model of the system, and $\overline{F}_c = F_c M_t^{-1}$ where M_t is the true mass. In contrast, the model used for control design is approximated as:

$$\ddot{z}(t) = f(z(t), \dot{z}(t), \eta(t)) - \hat{F}_c \tag{18}$$

$$f(z(t), \dot{z}(t), \eta(t)) = \left[F_d + F_{FK_{st}} + F_{FK_{dy}} - c(\omega_0)\dot{z}(t)\right]M^{-1}$$

$$\hat{F}_c = F_c M^{-1}$$

The calculation of the absorbed energy is [21]:

$$W = \int_o^t F_c\, \dot{z}(t)\, dt \tag{19}$$

3. Control Design

This section presents a sliding mode control (SMC) design, illustrated in Figure 3, for a heaving WEC based on the nonlinear differential equation model of Equation (16). Motivated by linear, complex conjugate control, the SMC reference trajectory is selected to match the frequency and phase of the excitation force. Since the WEC model is not linear, as assumed by complex conjugate control, it is recognized that this reference trajectory will not be optimal. Creating a real-time, energy extraction optimal reference trajectory is an open topic and well-suited for MPC applications. The reference velocity is then integrated to produce the reference displacement profile $z_r(t)$.

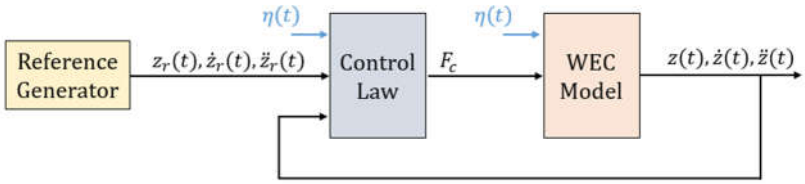

Figure 3. Configuration of proposed control schemes.

The sliding mode control is derived by first defining the sliding surface as:

$$s(\boldsymbol{z};t) = \dot{e}(t) + w\, e(t) \tag{20}$$

where $\boldsymbol{z}$ is the state vector, $\boldsymbol{z} = \left[z;\dot{z}\right]$ and w is a real-positive value that sets the rate at which the system converges to the sliding surface. The problem of tracking a given profile becomes equivalent to maintaining the stationarity conditions:

$$\dot{s}(t) = \ddot{e}(t) + w\,\dot{e}(t) = \ddot{z}_r(t) - \ddot{z}(t) + w\,\dot{e}(t) = 0 \tag{21}$$

Substituting Equation (18) into Equation (21), and solving for $\hat{F}_c$ gives the control law:

$$\hat{F}_c = f\big(z(t), \dot{z}(t), \eta(t)\big) - \big(\ddot{z}_r(t) + w\dot{e}(t)\big) \tag{22}$$

This control law will only work if the assumed form of the model is perfect and there are no disturbances. To account for these inevitable situations, Lyapunov's Direct method is used to augment the control law of Equation (22) to ensure stability.

The Lyapunov candidate function is selected as:

$$V(t) = \frac{1}{2}s^2(t) \tag{23}$$

For stability,

$$\dot{V} = s(t)\dot{s}(t) = s(t)\big(\ddot{z}_r(t) - \ddot{z}(t) + w\dot{e}(t)\big) < 0 \tag{24}$$

Substituting the true model, Equation (17) into Equation (24) gives:

$$\dot{V} = s(t)\big(\ddot{z}_r(t) - f_t\big(z(t), \dot{z}(t), \eta(t)\big) + \overline{F}_c + w\dot{e}(t)\big) < 0 \tag{25}$$

Next, substitute a modified version of the control law of Equation (22) where we have added a new term, $A_c sgn(s(t))$, that does not affect the stationary condition imposed earlier:

$$\hat{F}_c = -\ddot{z}_r(t) + f\big(z(t), \dot{z}(t), \eta(t)\big) - w\dot{e}(t) - A_c sgn(s(t)) \tag{26}$$

Furthermore, note that $\hat{F}_c \neq \overline{F}_c$ are related by $\overline{F}_c = \frac{M}{M_t}\hat{F}_c$. The time-dependency notation will be omitted for the following equations for brevity. We now have the stability condition:

$$\dot{V} = s\left(\ddot{z}_r - f_t(z,\dot{z},\eta) + \frac{M}{M_t}(-\ddot{z}_r + f(z,\dot{z},\eta) - w\dot{e} - A_c sgn(s)) + w\dot{e}\right) < 0 \quad (27)$$

or

$$A_c|s| > \ddot{z}_r - f(z,\dot{z},\eta) - w\dot{e} + \frac{M_t}{M}(-\ddot{z}_r + f_t(z,\dot{z},\eta) - w\dot{e}) \quad (28)$$

As long as A_c is sufficiently large to dominate the uncertainties on the right side of Equation (28), the system will be stable.

The discontinuous terms in the control of Equation (26) $A_c\ sgn(s(t))$ can cause chattering. This is eliminated by replacing the signum function with a hyperbolic tangent [22]. Then, the control law is interpolated by replacing $tanh(s(t))$ function by $s(t)/\Phi$ as:

$$F_c = F_d + F_{FK} - c(\omega_0)\dot{z}(t) - \left(\ddot{z}_r(t) + w\dot{e}(t)\right)M + A_c\ tanh(s(t)/\Phi) \quad (29)$$

where Φ is the boundary layer thickness.

The reference signal generator outputs the desired velocity profile of the WEC plant that is then integrated to obtain the desired displacement profile z_r. The control law takes as inputs the formed error signals, the desired acceleration profile $\ddot{z}_r$, the FK forces and the actual buoy displacement as in Equation (29). The control parameters A_c and Φ were chosen during the simulation process. As aforementioned, the reference velocity profile is designed to match the frequency and phase of the excitation force. As described in Reference [5], the optimum velocity condition requires:

$$\dot{z}_r(t) = \frac{F_{exc}(\omega_0)}{2\ c(\omega_0)} \quad (30)$$

To achieve this condition, phase control is needed so that the oscillation velocity $\dot{z}(t)$ is in phase with the excitation force and amplitude control to get a velocity amplitude of $|\dot{z}_r(t)| = |F_{exc}|/2c(\omega_0)$. However, this optimal condition leads to excessive motions of the device that would be infeasible in real-world applications. Therefore, the reference velocity profile is defined to be in phase with the excitation force with a suboptimal amplitude that varies for each sea state condition. Even though the WEC plant is nonlinear, in this study, the calculation of the reference velocity profile is based on the linear excitation force obtained from WAMIT [23].

To compare the results of the SMC, an approximate CCC [24] is used. Referring to the impedance matching principle [25], the optimal control force may be written as:

$$F_C^{opt}(\omega) = -Z_c^{opt}(\omega)\dot{z}(\omega) = -Z_i^*(\omega)\dot{z}(\omega) \quad (31)$$

where the optimal control impedance $Z_c^{opt}(\omega)$ must equal the complex-conjugate of the intrinsic impedance $Z_i = R_i(\omega) + iX(\omega)$ composed by the intrinsic resistance $R_i(\omega)$ and the intrinsic reactance $X_i(\omega)$. For monochromatic incident waves, this optimal force may be written in the time-domain as:

$$F_C^{opt}(t) = -M_c\ddot{z}(t) + c_c(\omega_0)\ \dot{z}(t) - k_c\ z(t) \quad (32)$$

For the optimal control, the controller values must equal the intrinsic values $M_c = M$, $c_c(\omega_0) = c(\omega_0)$, $k_c = k$, where k is the linear approximation of the static Froude-Krylov force. By cancellation, this control force gives the optimal response velocity shown in Equation (30) when the WEC model is assumed to be linear, and k is used instead of the nonlinear hydrostatic FK force. Since in this paper the WEC model is nonlinear, the

optimal control force using CCC was modified to obtain a perfect cancellation of the $F_{FK_{st}}$ as:

$$F_C^{opt}(t) = -M\ddot{z}(t) + c(\omega_0)\dot{z}(t) + F_{FK_{st}} \quad (33)$$

This control strategy used for comparison will be referred to as nonlinear complex-conjugate control $(NL - CCC)$ from this point on. The configuration of this control scheme is similar to that of the SMC shown in Figure 3. However, this control law only takes as inputs $z(t)$, $\dot{z}(t)$, $\ddot{z}(t)$, and, $\eta(t)$.

4. Simulation

As shown in previous studies [11], the significance of the Froude-Krylov nonlinear forces for a spherical body is great due to its varying cross-sectional area. The buoy parameters used in this simulation are listed in Table 1 and were chosen to resemble the parameters of a real device such as the WAVESTAR [26] device. The density of the body was chosen to be 500 kg/m^3 to make the draft of the buoy h_0 coincident with the center of gravity of the sphere, and the frequency-dependent hydrodynamic parameters were found by solving the radiation problem in WAMIT.

Table 1. Simulation parameters.

Parameter	Values
Buoy radius R	2.5 m
Buoy mass m	32,725 kg
Buoy draft h_d	2.5 m
Added mass $m_a(\omega_\infty)$	14,019 kg
Radiation damping $c(\omega_0)$	11,208 N/(m/s)
Water density ρ	1000 kg/m^3
Gravity constant g	9.81 m/s^2
Wave amplitude $A(\omega_0)$	0.5 m
Wave frequency ω_0	1.05 rad/s
Wavenumber $\chi(\omega_0)$	0.112
SMC convergence rate w	8
SMC coefficient ϕ	1000
SMC coefficient A_c	10 kN

The results showed in the following section correspond to the wave period of $T = 6$ s and $\omega_0 = 1.05$ rad/s. Therefore, the frequency-dependent parameters shown in Table 1 are based on this wave frequency.

Under the deep water assumption, the simulation was run for different monochromatic wave periods ranging from 3 to 9 s. In addition, the steepness of the wave S was kept constant at 0.018, which is the highest wave steepness under the linear waves assumption [18]. To maintain the wave steepness constant, the amplitude of the wave is related to the wavelength as $S = 2A/\lambda = 0.018$.

Table 2 shows the range of wave periods and their corresponding wavelength and wave amplitude.

Table 2. Wave characteristics and control parameters.

Wave Period (s)	3	4	5	6	7	8	9
Wavelength (m)	15	25	39	56	77	100	127
Wave Amplitude (m)	0.13	0.22	0.35	0.50	0.69	0.90	1.14
SMC Reference Amplitude (m)	0.6	1.1	1.8	2.19	2.14	2.05	1.9

The reference velocity profile in Equation (30) has been proven to be the optimum velocity [5] when using a linear approximation of the WEC, enabling maximum energy

absorption for a given buoy shape. However, this is not the case for this nonlinear WEC model where the $F_{FK_{dy}}$ is dependent on the incident wave elevation and the buoy displacement. Additionally, it is well-known that CCC magnifies the buoy's motion, driving the device to be either fully submerged or completely out of the water for certain wave periods. This undesirable behavior can be eliminated with the SMC by keeping the amplitude of the desired displacement bounded:

$$h_0 + S_f R - 2R > z_r > h_0 - S_f R \tag{34}$$

where S_f is a safety factor used to determine the maximum and minimum buoy height covered by water, as shown in Figure 4. Therefore, the amplitude of the desired displacement of the device was chosen to be a value within those limits. The SMC reference amplitude for each wave period is listed in Table 2.

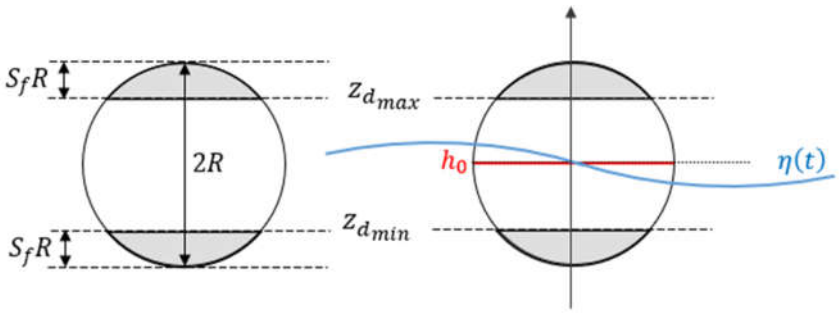

Figure 4. Spherical buoy limits of displacement.

5. Results

As aforementioned in Section 3, this paper compares the performance of the SMC against a complex-conjugate control (CCC) and a complex-conjugate control that includes the nonlinear static FK force in the control law (NL-CCC). The reference velocity used for the SMC is a cosine wave of the same frequency and phase as the linear hydrodynamic Froude-Krylov force obtained from WAMIT. To reduce the risk of driving the buoy completely out of the water or completely submerged into the water, a safety factor of $S_f = 10\%$ was used in the simulation, leaving 25 cm of clearance at the top and bottom of the spherical body.

The case shown in the results corresponds to a case where the CCC leads to a stable steady-state solution within the physical limits of the buoy. For higher wave periods, the solution with CCC would not reach steady-state. The maximum wave period at which the WEC controlled with the complex-conjugate control reached a steady-state solution within the physical limits of the buoy was at $T = 6s$. Therefore, that is the case that is shown in this paper. Figure 5 shows the relative displacement $z_d(t) - \eta(t)$ of the system using the different control strategies and the displacement limits to keep the buoy safe.

The relative displacement is kept within limits for the three control strategies used. The relative displacement when SMC is implemented is very well-behaved, and it takes advantage of the full range of motion available for the WEC. When CCC is implemented, there is a transient part for the first 15 s due to a 20-s ramp used to attenuate the overshoot caused by the control force. The relative displacement then reaches steady-state within the allowable range of motion. Note that the relative displacement with CCC is not in phase with the SMC. If the WEC plant were linear, the CCC and SMC would be in the phase. However, since the plant is nonlinear and the controller is a linear approximation, there is no perfect cancellation of the static FK force leading to a mismatch in relative displacements. Once the nonlinear static FK force is added to the CCC to form the NL-CCC, the relative displacement is in phase with the SMC. However, the amplitude of the relative displacement does not cover the full range of motion available since the minimum point at steady-state is already very close to the lower limit.

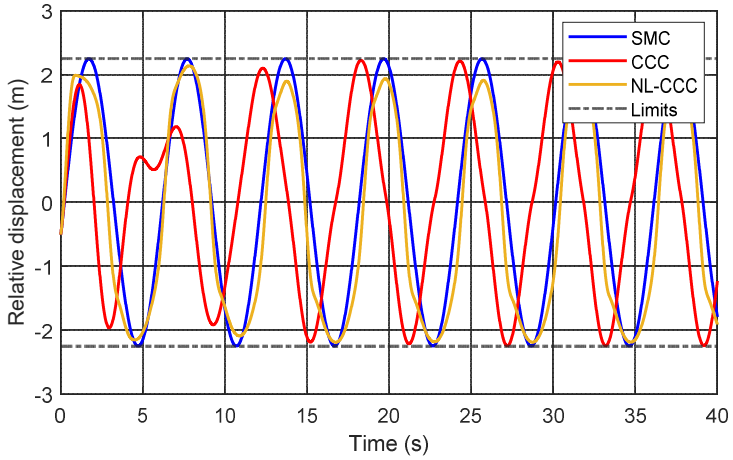

Figure 5. Relative displacement $z_d(t) - \eta(t)$ of the WEC when implementing SMC, CCC, and NL−CCC at $T = 6$ s.

The energy absorbed by the system when using the three control strategies and the control force used is shown in Figure 6. From this figure, it can be observed that the CCC performance is very poor compared to the SMC and the NL-CCC performance. This low energy absorption is caused by the very limited control force needed to maintain the WECs motion bounded. On the contrary, the energy absorbed when using SMC and NL-CCC are similar, with the SMC being slightly higher. However, the NL-CCC required a higher magnitude control force than the SMC to achieve slightly less energy absorption.

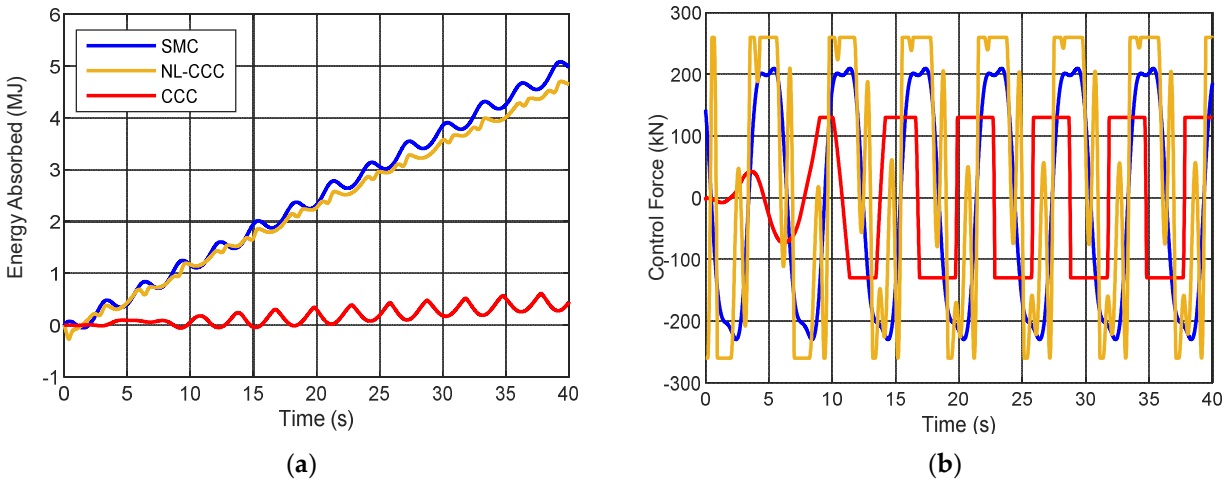

(**a**) (**b**)

Figure 6. Absorbed energy (**a**) and control force (**b**) when implementing SMC, NL−CCC and CCC at $T = 6$ s.

Additionally, the SMC control force is a continuous function that does not need to be clipped in order to keep the WEC safe. On the other hand, the control force of CCC and NL-CCC are both saturated, causing discontinuities in the force. Furthermore, in order to maintain the WEC bounded in the safe range of motion, the control force of CCC and NL-CCC has to be limited at a different value for each sea state. While, for the SMC, this is not necessary, since the motion of the WEC is determined by the reference signals.

Although, in this case, the difference between the energy absorbed by the SMC and NL-CCC is very close, that is not the case for higher wave periods. The power absorbed by the WEC when using the three control strategies at different wave periods is shown in Figure 7. As the wave period increases, because the wave steepness is kept constant, the wave height increases. With increasing the wave amplitudes, the WECs displacement is significantly different from the wave elevation. Therefore, the mean wetted surface

is significantly different from the instantaneous wetted surface used in this nonlinear approach, making the nonlinear Froude-Krylov forces very significant. Hence, when using a linear control strategy such as the CCC for higher wave periods, the control force must be highly limited in order to keep the WEC safe, reducing the power absorption significantly. Similarly, when using the NL-CCC, even though the nonlinear static FK force is incorporated in the controller, the nonlinear dynamic FK becomes very relevant; therefore, the control force must be limited to keep the WEC bounded. The hydrodynamic parameters used for the wave periods shown in this figure are shown in Appendix A.

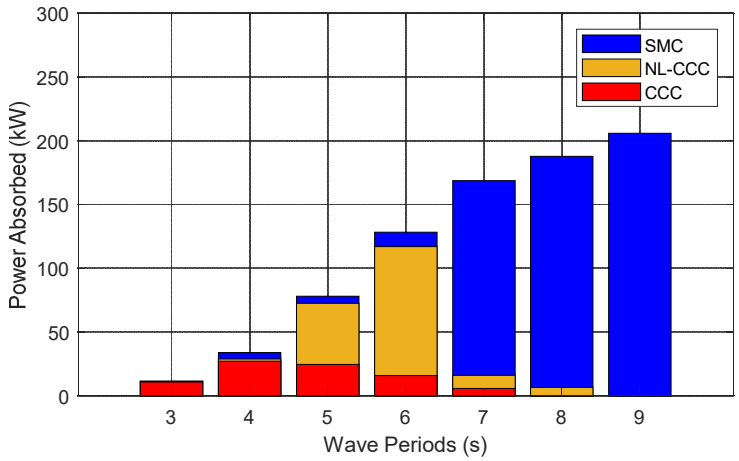

Figure 7. Absorbed Power for the different control strategies with varying wave periods and constant steepness of regular waves.

The difference in power absorption between the three strategies is very small in the shorter wave periods range, particularly between the SMC and the NL-CCC. Except for the WECs natural frequency of $\omega_n = 2.43\frac{\text{rad}}{\text{s}}$, where, again, the CCC and NL-CCC control strategies need to be very limited to avoid extreme excursions of the WEC. Due to the SMC's ability to track the reference signal and assuming that there are no constraints in the control force for the longer wave periods, the power absorption outperforms that of CCC and NL-CCC.

The sliding mode controller is additionally very robust against modeling uncertainties or disturbances experienced by the system. From the parameters in Equation (29), a source of uncertainty could be the terms in the radiation force ($m_a(\omega_\infty)$, $c(\omega_0)$), and the wavenumber $\chi(\omega_0)$ in the dynamic Froude-Krylov force. These parameters can vary due to an error in the system identification, or the device is biofouled, the system is disturbed, etc.

The exact model assumes 100% certainty of the three parameters mentioned above and the perturbed model assumes 50% uncertainty of the three parameters simultaneously. In Figure 8 is shown a line with slope $-w$ in blue, and the sliding surface $s(t)$ in red for the perturbed model. In Figure 8a, the SMC coefficient A_c of the term $A_c \tan \mathrm{h}(s/\phi)$ in Equation (29) was kept the same as the value used in the exact model 10 kN. However, as seen from the figure, the initial loop starts at (0;0) due to matching initial conditions between the system states and the reference states, then the sliding surface keeps looping around the blue line, increasing in magnitude. This indicates that the error is not bounded, and therefore, the system could go unstable. Therefore, A_c was increased to 100 MN to handle the uncertainty errors. The sliding surface shown in red in Figure 8b forms a closed contour and loops around it, meaning that the error is controlled and will not go unbounded. Hence, when the model is not exact, the A_c needs to be increased. For different wave periods, and depending on the modeling error or disturbances, the SMC coefficient A_c might have to be adjusted to ensure the WEC is tracking the reference signals without much deviation.

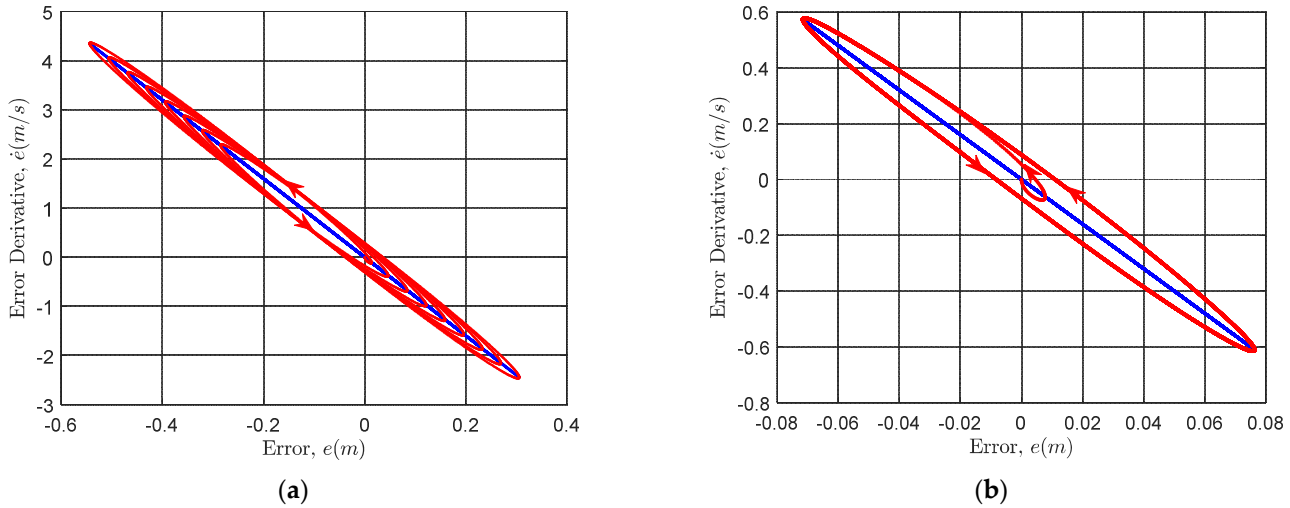

Figure 8. Phase−plane plot of sliding surface $s(t)$ with SMC coefficient of $A_c = 10\ kN$ on the left (**a**), and $A_c = 100\ MN$ on the right (**b**).

Figure 9a shows the error between the reference displacement and the WEC displacement for the exact and perturbed model with $A_c = 100\ MN$. The error for the exact model is close to 0, while, for the perturbed model, it oscillates between $\pm 7.7610^{-2}$ m which is approximately a 3.5% error. To keep this error between a 5% error margin, the SMC coefficient A_c had to be increased. As mentioned in Section 3, the higher the magnitude of this coefficient, the more robust the SMC is. However, as seen from the control force in Figure 9b, the increase in its magnitude barely affected the control force. This behavior is because the term $A_c \tan \mathrm{h}(s(t))$ of the control law offsets the difference in the terms with uncertainties between the exact and perturbed model.

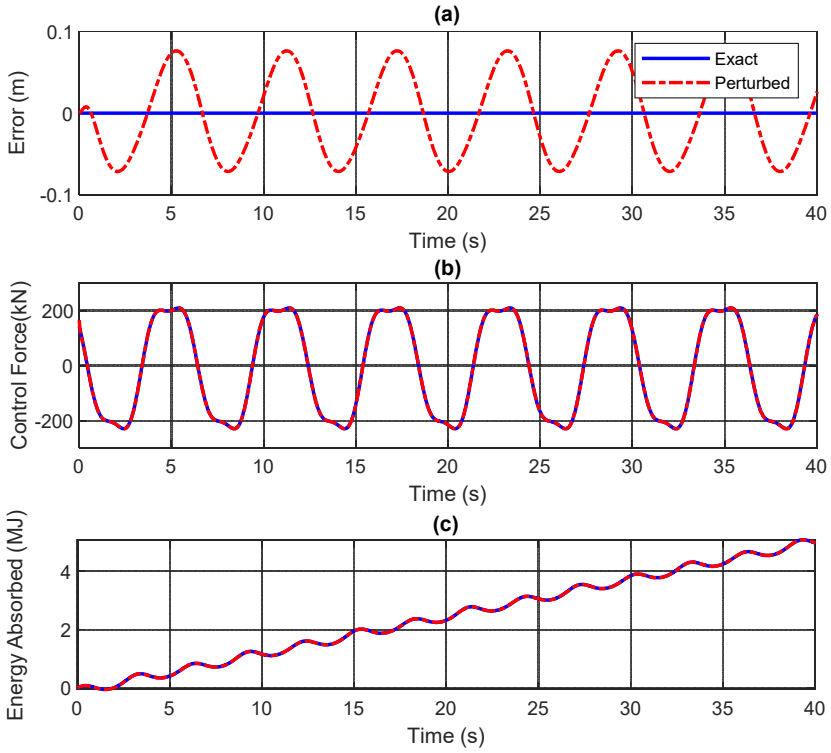

Figure 9. (**a**) Displacement error between reference and WEC displacement, (**b**) Control Force, and (**c**) Energy Absorption of the Exact Model and the Perturbed Model.

The energy absorption shown in Figure 9c does not seem to be influenced by the slight error in the WEC's displacement and the control force. Both the exact and perturbed models needed almost the same control force to deliver equivalent energy absorption. Therefore, the SMC has proven to work very well in systems prone to modeling errors and environmental disturbances such as wave energy converters.

6. Conclusions

Three different control strategies have been presented and applied to a spherical heaving point absorber wave energy converter. These control strategies have shown promising results when used in linear models of WECs. However, it has been shown that linear model approximations lead to inaccurate models when there is a significant difference between WEC displacement and wave elevation. Therefore, this paper presented a sliding mode controller applied to a nonlinear WEC model. This plant incorporates the algebraic nonlinear static and dynamic Froude-Krylov forces.

The SMC was compared to a complex-conjugate control, and a variation of this complex-conjugate control with a nonlinear static FK force term. The controllers aimed to obtain the higher power possible of all control strategies tested while maintaining the WEC within a safe range of motion. The simulation was done using linear and regular waves at a constant wave steepness of 0.018.

It was found that the proposed SMC successfully tracked the reference signals given at all of the wave periods tested. This was achieved by a continuous control force without constraints in magnitude, which would reduce the chance of failure in real-world applications by making the device more reliable. Furthermore, it was shown that the control force does not need to be limited at different values for each sea-state in order to keep the WEC in the safe range of motion, as long as the reference signals fall within those safe bounds.

The sliding mode controller allowed the maximum energy absorption between the control strategies tested at all of the wave periods. At lower wave periods, this was done by requiring less control force than the NL-CCC, and at higher wave periods, where the nonlinearities become very significant, the energy absorbed when using SMC proved to be substantially greater than when using CCC and NL-CCC. In addition, the sliding mode controller allows for the use of any desired reference signal, meaning that if there already exists a path that would deliver the optimal absorbed energy, it could just be used as a reference in the SMC and achieve optimal performance.

Furthermore, the SMC was simulated with modeling errors of 50% in the radiation force, and 50% error in the wavenumber used to calculate the nonlinear dynamic FK force. Despite these uncertainties, the SMC kept the wave energy converter in the tracking reference while using a continuous control force and delivering the same energy absorbed as the exact system. This robustness characteristic of sliding mode controllers is ideal for marine devices where the system parameters may vary over time due to aging, biofouling, corrosion, etc.

Future work includes extending the proposed sliding mode controller to work in irregular waves to test for more real-world scenarios. In addition, the designed controller can be experimentally validated by using a scaled-down point absorber hardware in the wave tank.

This paper used purely heaving point absorbers due to the computationally efficient algebraic nonlinear Froude-Krylov forces derived from Giorgi et al.'s work. However, this could be extended to more degrees of freedom in the future, where numerical approaches need to be used to solve the Froude-Krylov integrals, as explained in Reference [13].

Author Contributions: Methodology, T.D.G. and G.G.P.; Resources, G.G.P. and E.A.; Software, T.D.G.; Supervision, G.G.P.; Validation, T.D.G.; Visualization, T.D.G.; Writing—original draft, T.D.G.; and Writing—review and editing, E.A. and W.W.W. All authors have read and agreed to the published version of the manuscript.

Funding: This research received no external funding.

Institutional Review Board Statement: Not applicable.

Informed Consent Statement: Not applicable.

Data Availability Statement: Publicly available datasets were analyzed in this study. This data can be found here: https://github.com/tsdemont/Results_JMSE_1349687 (accessed on 25 August 2021).

Conflicts of Interest: The authors declare no conflict of interest.

Appendix A

The hydrodynamic parameters used in the simulation for each wave period shown in Figure 7 are listed in Table A1. These parameters were obtained from WAMIT [23] for the spherical body with parameters listed in Table 1.

In addition, the amplitude of the SMC displacement reference used for each wave period is shown in Table 2. The energy absorbed by the WEC shown in Figure 7 was obtained using all of these parameters.

Table A1. Hydrodynamic parameters for different wave periods.

Wave Period (s)	3	4	5	6	7	8	9
Wave frequency ω_0 (rad/s)	2	1.57	1.26	1.05	0.89	0.78	0.7
Wavenumber $\chi(\omega_0)$	0.42	0.25	0.16	0.11	0.082	0.063	0.05
Radiation damping $c(\omega_0)$ (N/(m/s))	16.19	16.81	14.35	11.21	8.51	6.64	5.02

References

1. Gunn, K.; Stock-Williams, C. Quantifying the potential global market for wave power. In Proceedings of the 4th International Conference on Ocean Engineering (ICOE 2012), Dublin, Ireland, 17–19 October 2012; pp. 1–7. Available online: https://www.icoe-conference.com/publication/quantifying_the_potential_global_market_for_wave_power/ (accessed on 25 August 2021).
2. LiVecchi, A.; Copping, A.; Jenne, D.; Gorton, A.; Preus, R.; Gill, G.; Robichaud, R.; Green, R.; Geerlofs, S.; Gore, S.; et al. *Powering the Blue Economy: Exploring Opportunities for Marine Renewable Energy in Maritime Markets*; U.S. Department of Energy Office of Energy Efficiency and Renewable Energy: Washington, DC, USA, 2019; pp. 158–163. Available online: https://www.energy.gov/sites/prod/files/2019/03/f61/73355.pdf (accessed on 25 August 2021).
3. Faÿ, F.-X.; Henriques, J.C.; Kelly, J.; Mueller, M.; Abusara, M.; Sheng, W.; Marcos, M. Comparative assessment of control strategies for the biradial turbine in the Mutriku OWC plant. *Renew. Energy* **2020**, *146*, 2766–2784. [CrossRef]
4. Maria-Arenas, A.; Garrido, A.J.; Rusu, E.; Garrido, I. Control Strategies Applied to Wave Energy Converters: State of the Art. *Energies* **2019**, *12*, 3115. [CrossRef]
5. Falnes, J.; Kurniawan, A. *Ocean Waves and Oscillating Systems: Linear Interactions Including Wave-Energy Extraction*; Cambridge University Press: Cambridge, UK, 2020; ISBN 978-1-108-48166-3.
6. Babarit, A.; Clément, A.H. Optimal latching control of a wave energy device in regular and irregular waves. *Appl. Ocean Res.* **2006**, *28*, 77–91. [CrossRef]
7. Todalshaug, J.; Bjarte-Larsson, T.; Falnes, J. Optimum Reactive Control and Control by Latching of a Wave-Absorbing Semisubmerged Heaving Sphere. In Proceedings of the International Conference on Offshore Mechanics and Arctic Engineering, Oslo, Norway, 23–28 June 2002; Volume 4, pp. 415–423. [CrossRef]
8. Cretel, J.; Lewis, A.W.; Lightbody, G.; Thomas, G.P. An Application of Model Predictive Control to a Wave Energy Point Absorber. *IFAC Proc. Vol.* **2010**, *43*, 267–272. [CrossRef]
9. Cummins, W.E. *United States Department of the Navy. The Impulse Response Functions and Ship Motions*; David Taylor Model Basin; United States Department of the Navy: Bethesda, MD, USA, 1962.
10. Windt, C.; Faedo, N.; Penalba, M.; Dias, F.; Ringwood, J.V. Reactive control of wave energy devices—The modelling paradox. *Appl. Ocean Res.* **2021**, *109*, 102574. [CrossRef]
11. Merigaud, A.; Gilloteaux, J.; Ringwood, J. A Nonlinear Extension for Linear Boundary Element Methods in Wave Energy Device Modelling. In Proceedings of the International Conference on Offshore Mechanics and Arctic Engineering, Rio de Janeiro, Brazil, 1–6 July 2012; Volume 4. [CrossRef]
12. Giorgi, G.; Ringwood, J.V. Nonlinear Froude-Krylov and viscous drag representations for wave energy converters in the computation/fidelity continuum. *Ocean Eng.* **2017**, *141*, 164–175. [CrossRef]
13. Giorgi, G.; Ringwood, J.V. Computationally efficient nonlinear Froude–Krylov force calculations for heaving axisymmetric wave energy point absorbers. *J. Ocean Eng. Mar. Energy* **2017**, *3*, 21–33. [CrossRef]

14. Levant, A.; Levantovsky, L. Sliding Order and Sliding Accuracy in Sliding Mode Control. *Int. J. Control NT J CONTR* **1993**, *58*, 1247–1263. [CrossRef]
15. Gaebele, D.T.; Magaña, M.E.; Brekken, T.K.A.; Henriques, J.C.C.; Carrelhas, A.A.D.; Gato, L.M.C. Second Order Sliding Mode Control of Oscillating Water Column Wave Energy Converters for Power Improvement. *IEEE Trans. Sustain. Energy* **2021**, *12*, 1151–1160. [CrossRef]
16. Vu, M.T.; Le, T.-H.; Thanh, H.L.N.N.; Huynh, T.-T.; Van, M.; Hoang, Q.-D.; Do, T.D. Robust Position Control of an Over-actuated Underwater Vehicle under Model Uncertainties and Ocean Current Effects Using Dynamic Sliding Mode Surface and Optimal Allocation Control. *Sensors* **2021**, *21*, 747. [CrossRef] [PubMed]
17. Wahyudie, A.; Jama, M.A.; Assi, A.; Noura, H. Sliding mode and fuzzy logic control for heaving wave energy converter. In Proceedings of the 52nd IEEE Conference on Decision and Control, Firenze, Italy, 10–13 December 2013; pp. 1671–1677.
18. Mehaute, B.L. *An Introduction to Hydrodynamics and Water Waves*; Springer Study Edition; Springer: Berlin/Heidelberg, Germany, 1976; ISBN 978-3-642-85567-2.
19. Korde, U.A.; Ringwood, J. *Hydrodynamic Control of Wave Energy Devices*; Cambridge University Press: Cambridge, UK, 2016.
20. Todalshaug, J.H. Hydrodynamics of WECs. In *Handbook of Ocean Wave Energy*; Pecher, A., Kofoed, J.P., Eds.; Ocean Engineering & Oceanography; Springer International Publishing: Cham, Switzerland, 2017; pp. 139–158; ISBN 978-3-319-39889-1.
21. Falnes, J. A review of wave-energy extraction. *Mar. Struct.* **2007**, *20*, 185–201. [CrossRef]
22. Slotine, J.-J.E.; Li, W. *Applied Nonlinear Control*; Prentice Hall: Englewood Cliffs, NJ, USA, 1991; ISBN 978-0-13-040890-7.
23. Wamit, Inc. The State of the Art in Wave Interaction Analysis. Available online: https://www.wamit.com/ (accessed on 24 July 2021).
24. Todalshaug, J.; Falnes, J.; Moan, T. A Comparison of Selected Strategies for Adaptive Control of Wave Energy Converters. *J. Offshore Mech. Arct. Eng.* **2011**, *133*, 031101.
25. Nebel, P. Maximizing the Efficiency of Wave-Energy Plant Using Complex-Conjugate Control. *Proc. Inst. Mech. Eng. Part J. Syst. Control Eng.* **1992**, *206*, 225–236. [CrossRef]
26. Wavestar. Available online: http://wavestarenergy.com/ (accessed on 24 July 2021).